



Phase-stabilized complex-decorrelation angiography

XIANG WEI,^{1,2} TRISTAN T. HORMEL,¹ AND YALI JIA^{1,2,*}

¹Casey Eye Institute, Oregon Health and Science University, Portland, Oregon 97239, USA

²Department of Biomedical Engineering, Oregon Health and Science University, Portland, Oregon 97239, USA

*jiaya@ohsu.edu

Abstract: In this study, we developed a novel phase-stabilized complex-decorrelation (PSCD) optical coherence tomography (OCT) angiography (OCTA) method that can generate high quality OCTA images. This method has been validated using three different types of OCT systems and compared with conventional complex- and amplitude-based OCTA algorithms. Our results suggest that in combination with a pre-processing phase stabilization method, the PSCD method is insensitive to bulk motion phase shifts, less dependent on OCT reflectance than conventional complex methods and demonstrates extended dynamic range of flow signal, in contrast to other two methods.

© 2021 Optical Society of America under the terms of the [OSA Open Access Publishing Agreement](#)

1. Introduction

Optical coherence tomography (OCT) angiography (OCTA) is a recently developed vascular imaging method used in many experimental and clinical applications [1–5]. As a non-invasive method, OCTA can provide high-sensitivity, high-resolution, three-dimensional angiograms with minimal side effects [6]. OCTA is generated by measuring motion contrast in the reflectance signal encoded in the raw spectrum data acquired by the OCT system. The motion contrast is extracted by measuring changes across multiple repeated scans at the same position [1–3,7]. At the physical scale of blood cells, contrast in the OCT reflectance signal is dominated by speckle. While the speckle pattern recorded in static tissue will not change between scans, moving blood cells will generate a time-varying effect that can be measured to produce angiographic images. The OCT reflectance signal is complex, containing both amplitude and phase components. Depending on which signal is processed, OCTA systems can be described as either amplitude-, phase-, or (in the case where both signals are processed to form the image) complex-based. Both change in phase and amplitude can ultimately be viewed as deriving from the changing speckle pattern [8–12]. The choice of signal to process is not immaterial, as it determines flow signal sensitivity, dynamic range, and dependency on signal strength of scan quality [13–15].

Each signal offers some advantages and disadvantages. The phase signal is the most sensitive, being capable of detecting only slight variation in the reflectance signal, and in certain circumstances it can also derive flow velocity [2,5]. However, the extreme sensitivity of the phase signal also means that it is vulnerable to system- and bulk motion-induced phase shift noise, so phase-based OCTA processing requires phase stabilization approaches [2,3,16–18] to remove phase shift unrelated to blood flow. Amplitude-based OCTA loses this extreme sensitivity to motion, but can consequently forego phase stabilization and bulk motion correction, and is incapable of measuring flow speed via Doppler shift. Loss of sensitivity may seem problematic, but this loss is rarely material since amplitude-based approaches have sufficient sensitivity to detect blood flow in capillaries, which is the minimum sensitivity required from a clinical or anatomic perspective. Finally, complex-based OCTA has the theoretical advantage of utilizing all of the information available in the reflectance signal. But, like phase-based methods, phase stabilization or compensation is a critical requirement.

In previous work, we introduced an efficient bulk motion phase compensation technique for spectral domain OCTA devices [16]. Spectral domain OCT has the advantages of high axial resolution and phase stability. The scanning speed is usually less than 250 kHz [19–21]. However, for wide-field applications, faster scanning speeds are critical. The fastest OCTA devices are swept-source, rather than spectral domain, instruments [22,23]. And while our previous approach performed well in comparison to other state-of-the-art histogram-based phase compensation approaches [2,24], it cannot be applied to swept-source OCTA devices. The main issue is trigger jitter, a source of noise unique to swept-source devices in OCTA technology. Trigger jitter is caused by minor sweep triggering time differences. The slight difference will make each spectrum measurement lead or lag a small bit, which causes a wave-number-dependent phase shift along the axial direction. This kind of artifact can happen with any type of swept source illumination. Methods either based on hardware [25] or post processing algorithms [17,18,26,27] have been developed to remove trigger jitter artifacts. Many phase compensation algorithms assume a constant phase across imaging depth, but the random electronic noise introduced by trigger jitter violates this assumption [26].

In this study we introduce a phase compensation approach to perform on any OCTA device, including swept-source instruments. We also introduce a new OCTA flow detection metric, which we call phase-stabilized complex-decorrelation angiography (PSCDA). We demonstrate that PSCDA can efficiently produce clean, high dynamic range angiograms from multiple devices. We also quantitatively and qualitatively benchmark the performance of the PSCDA against two other leading OCTA processing techniques: split-spectrum amplitude-decorrelation angiography (SSADA) [1] and complex difference (CDIF) angiography.

2. Methods

2.1. Phase-stabilized complex decorrelation

In phase- and complex-based OCTA signal generation an effective means to stabilize the phase signal and remove phase noise can greatly improve the signal-to-noise ratio for flow detection. The phase portion of the spectral domain OCT signal can be represented as [3]

$$\phi(x, z) = \phi_P(x, z) + \phi_B(x, z) + \phi_M(x, z). \quad (1)$$

Here, ϕ_P is the phase shift caused by the moving red blood cells in vessels, ϕ_B is the bulk motion phase shift caused by involuntary motion, and ϕ_M is the system modulation phase shift that is mainly contributed by the movement of the mechanical scanner at scanning location (x, z) . The $\phi_B(x, z)$ and $\phi_M(x, z)$ terms represent the phase noise we wish to remove; this can be accomplished with one of several phase compensation algorithms [2,3,16]. In this study, we used our previously developed high-performance, robust standard-deviation-based bulk motion compensation method to remove the phase noise [16]. The bulk motion phase is calculated by using the pixel-wise standard deviation of the variance images constructed from two repeated scans with a tunable phase introduced:

$$\Delta\phi_{B+M} = \tan_4^{-1} \left(\frac{v_1 - v_3}{v_2 - v_0} \right). \quad (2)$$

Here, the \tan_4^{-1} is the four-quadrant inverse tangent, and the variance v_j is calculated according to

$$v_j = \text{std} \left(\left| C_n(x, z) - C_{n+1}(x, z) \cdot \exp(-i \cdot j \cdot \frac{\pi}{2}) \right|^2 \right) \quad (3)$$

where $\text{std}(\bullet)$ is the standard deviation, C is the complex signal, v_j is indexed by j , and n is the scan index. This method can deliver a highly accurate bulk motion compensation result and requires minimal computational resources.

Phase stabilization is more complicated in swept source systems because trigger jitter in these instruments introduces an additional phase shift that must be corrected before bulk motion compensation. Compared to perfectly controlled triggering timing, the actual triggering time can randomly lead or lag a small amount of time Δt (usually several nanoseconds), yielding a phase contribution to the wavenumber k :

$$\phi_t = \delta k \cdot z \quad (4)$$

To remove this contribution to the phase the averaged phase difference gradient can be calculated across each A-line to estimate δk in Eq. (4), or the spectrum time shift between two repeated scans can be aligned [17,18]. In this study, we follow a spectrum-amplitude based method to remove the trigger jitter [17]. The time shift between repeated A-scans was estimated using cross-correlation. After obtaining the time shift, repeated A-scans were shifted accordingly to eliminate any time shift caused by the trigger jitter.

After phase stabilization, either the phase- or complex-based OCTA signal can be extracted. The complex signal at each location can be represented by two vectors, these two vectors have both amplitude and phase differences.

The vectors' variance can be calculated using amplitude or phase only, however, both of options will lose some information. Here, we combined the phase and amplitude variance signals by calculating a summary arc length measure between two vectors (green arcs in Fig. 1).

$$ARC = (|\vec{A}_n(x, z)| + |\vec{A}_{n+1}(x, z)|) \cdot \theta' \quad (5)$$

Here, $\vec{A}_n(x, z)$ and $\vec{A}_{n+1}(x, z)$ represent two measurements from repeated scans. The ARC length can then be normalized using the vectors' summed magnitude

$$ARC_{norm} = \frac{(|\vec{A}_n(x, z)| + |\vec{A}_{n+1}(x, z)|) \cdot \theta'}{\sqrt{A_n^2(x, z) + A_{n+1}^2(x, z)}} \quad (6)$$

We then calculate the square of ARC_{norm} to remove the square root sign and the absolute value sign. The novel phase-stabilized complex-decorrelation metric to extract the OCTA signal is then:

$$PSCD = \sum_{n=1}^{N-1} \frac{[A_n(x, z) + A_{n+1}(x, z)]^2 \cdot \theta'^2}{A_n^2(x, z) + A_{n+1}^2(x, z)} \quad (7)$$

Here, A_n and A_{n+1} represent the amplitude signal from two repeated scans, N is the number of repeated scans, and $\theta'_n(x, z) = \phi_n - \phi_{n+1}$ represents the phase difference between two repeated

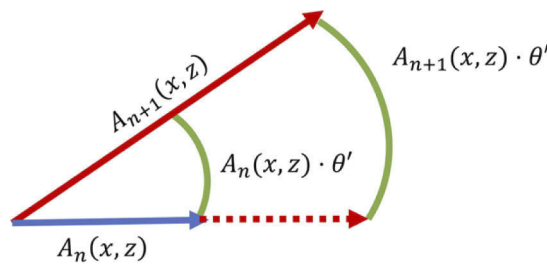


Fig. 1. Complex signals represented by two vectors. Here, the blue arrow represents the complex signal measured in a scan, and the red arrow represents the complex signal from a repeated scan. The dotted arrow is the amplitude difference and the green arcs are the arc length.

scans after bulk motion compensation and trigger jitter removal, which can be calculated as

$$\theta'_n(x, z) = \left| \tan^{-1} \frac{\text{imag}(C_n(x, z) \cdot C_{n+1}(x, z)^*)}{\text{real}(C_n(x, z) \cdot C_{n+1}(x, z)^*)} \right|, \quad (8)$$

where C_n and C_{n+1} represent the complex signal from two repeated scans, \tan^{-1} represents the inverse tangent, “*imag*” is the imaginary part of the complex variable, and “*real*” is the real part. By using this method, the amplitude signal is normalized according to the tissue reflectance, removing the reflectance dependence on the PSCD signal, and the inclusion of the θ_n term can further enhance the flow signal and increase the dynamic range.

2.2. Complex difference method

In complex difference (CDIF) methods the OCTA signal is generated by calculating the absolute difference between two repeated scans [24]

$$\text{OCTA}_{\text{CD}} = |C_n(x, z) - C_{n+1}(x, z)|. \quad (9)$$

Here, C_n and C_{n+1} are the complex signals generated from two repeated B-scans at the same location. In terms of amplitude $A_n(x, z)$ and the phase part $\phi_n(x, z)$, Eq. (7) can be written as

$$\text{OCTA}_{\text{CD}} = |A_n(x, z) \cdot \exp(i \cdot \phi_n(x, z)) - A_{n+1}(x, z) \cdot \exp(i \cdot \phi_{n+1}(x, z))| \quad (10)$$

Optical microangiography (OMAG) is a prominent example of a CDIF approach. Like split-spectrum amplitude-decorrelation angiography (SSADA), it is an efficient OCTA algorithm that has been commercialized [3].

2.3. SSADA

Amplitude methods can also generate high quality OCTA images. SSADA applies multiple spectral splits to enhance the signal as [1]

$$\text{SSADA} = 1 - \frac{1}{N-1} \frac{1}{M} \sum_{n=1}^{N-1} \sum_{m=1}^M \frac{2 \cdot A_{n,m}(x, z) \cdot A_{n+1,m}(x, z)}{A_{n,m}(x, z)^2 + A_{n+1,m}(x, z)^2}, \quad (11)$$

where $A_{n,m}(x, z)$ represents the n-th repeated OCT B-scan amplitude signal at position x and z , m represents m-th split spectrum. N represents the number of repeated scans at the same position and M represents the number of split spectrums. In this study, to maximally enhance the OCTA signal, we are using 11 spectral splits [28].

2.4. OCT systems

We tested our PSCD signal generation algorithm using three different instruments. The first (the “400-kHz system” hereafter) was a previously developed high-speed, wide-field swept-source OCT prototype [29]. A 400-kHz “ping-pong” laser (Axsun Technologies Inc.) with a center wavelength of 1060 nm with a 100 nm bandwidth was used. The system provides a lateral resolution of 10 μm and axial resolution of 5 μm . Graphics processing unit (GPU)-based real-time OCT/OCTA data processing software [30] was also developed for the system. The software also integrated a OCTA based self-tracking method [31] to remove blinks and microsaccades by rescanning the artifact-affected area in real-time. A 75-degree field of view can be achieved with this system. The second OCT system (the “visible-light system”) is a 50-kHz spectral domain prototype primarily developed for rodent imaging [32], working in the visible band with a center wavelength of 560 nm and a 100 nm bandwidth. The system provides 1.2 μm axial resolution and 6- μm lateral resolution. GPU-based OCT/OCTA data acquisition software was

also developed for the system to monitor the OCT and OCTA image quality in real-time [30]. We also assessed algorithm performance on a commercial 70-kHz spectral domain OCT system (RTVue-XR Avanti; Optovue, Inc., Fremont, CA; the “commercial system”). This system has a center wavelength of 840 nm, axial resolution of 5 μm and lateral resolution of 10 μm . All the experimental procedures were approved by Oregon Health and Science University’s (OHSU) Institutional Review Board/Ethics Committee.

2.5. Flow phantom experiment

A flow phantom setup that is similar to our previous study [15] has been made using 250- μm inner diameter clear glass tubing. A syringe pump enables controlled flow variation in the tubing with speeds ranging from 0 to 6 mm/s. Bovine blood was used as the fluid in these experiments. All flow phantom data was acquired with the 400-kHz swept source OCT system.

2.6. Rodent imaging

Brown Norway rats were first anesthetized in a sealed chamber with 5% isoflurane for 10 minutes. During the imaging session, oxygen gas with 2.5% isoflurane at a flow rate of 1L/min is used for inhalation. The exhaust isoflurane is absorbed using a gas filter (OMNICON F/air, Bickford). The animal body temperature is maintained using 38.5 °C using a water-warming blanket. All the experimental procedures were approved by the Institutional Animal Care and Use Committee (IACUC) of OHSU. 2.1 \times 2.1-mm OCT scan volumes were acquired. 512 A-lines were sampled to obtain a single B-scan. Three repeated B-scans were captured at a fixed position before proceeding to the next sampling location. A total of 512 locations were scanned. The brightness and contrast of these images were adjusted by normalize using the pixel value between 5% to 95% of the total pixels value. *En face* OCT reflectance images were also generated.

2.7. Human imaging

Fourteen patients’ eyes were imaged using a 70-kHz commercial OCT system. These images were acquired by a professional OCT operator. The image size is 3 \times 3 mm, centered at the fovea. Each contains 304 A-lines in each B-scan, and each A-line contained 2048 pixels. Two repeated B-scans were acquired at each cross-sectional position. A total of 304 positions were scanned across the total 3 mm scanning length. The generated OCT and OCTA images were segmented using our previously developed automatic segmentation software [33]. *En face* OCTA images were then generated using maximum projection [34]. A custom color map was applied to better illustrate the OCTA image.

3. Results

3.1. Phase stabilization

To verify the performance of our phase stabilization procedure, we acquired flow phantom and human retinal images using the 400-kHz system. First, we generated an uncompensated phase difference image. The phase difference images are calculated directly from two repeated B-scans acquired at the same lateral position. Both the flow phantom image (Fig. 2(A)) and the wide-field retinal image (Fig. 2(B)) contain significant phase noise. The major noise contributions to the flow phantom image are from the system modulation caused by the rotation of the galvo scanner and from trigger jitter. The reflectance signal in flow phantom experiments is small due to the low reflectivity of the materials, which causes it to be dominated by noise. The random phase background noise level is therefore high in the flow phantom phase difference data. Phase noise in the retinal image also includes a contribution from involuntary subject movement (e.g., due to ocular pulsation). After applying the phase stabilization algorithm in our PSCD method both the phase stabilized flow phantom (Fig. 2(C)) and retinal phase difference images (Fig. 2(D))

have an even phase background that is close to zero. Our algorithm can effectively remove the background phase noise even when it is large. This effectiveness can be demonstrated using an axial averaged phase plot (Fig. 2).

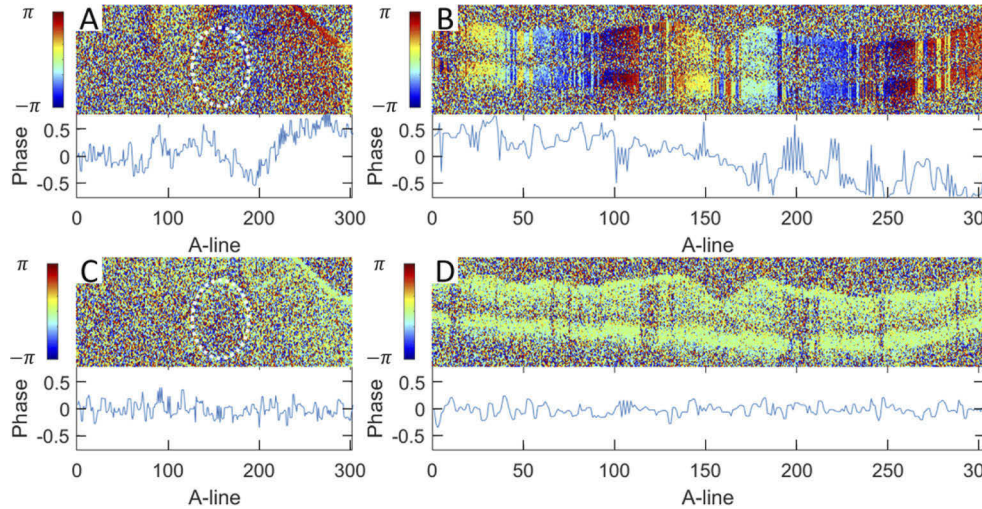


Fig. 2. Phase difference plots before and after applying the phase stabilization method. (A) Flow phantom phase difference image without phase stabilization, (B) 12-mm wide-field OCT phase difference image without phase stabilization, (C-D) equivalent images with phase stabilization. The mean phase difference value along the axial direction is plotted under each image. With phase stabilization, the phase difference values in (C) and (D) are consistently near zero, indicating good performance. Dotted white circles indicate the tube position in (A, C).

3.2. Dynamic range

The dynamic range of flow detection is a key parameter in OCTA technology that is controlled by both the device's scanning interval pattern [15] and the OCTA generation algorithm. To assess the dynamic range of the proposed PSCD method we performed a flow phantom experiment. For comparison's sake, we also processed our data using the CDIF technique [24] and SSADA technique [1]. The flow phantom apparatus was placed at a small angle to the perpendicular direction of the scanning laser beam. The OCT sample beam was scanned across a 1 mm wide cross-section of the glass tubing. 300 A-lines were acquired for each B-scan, and a total of 128 continuous B-scans were acquired from this single position. The OCTA images were generated using the adjacent B-scans with a scanning interval of 1.5 ms.

All the PSCD, CDIF and SSADA methods can highlight the flow signal in the flow phantom and remove the static background signal (Fig. 3(D), E, F)). Both the complex algorithms used the same standard deviation based bulk motion compensation algorithm to remove the system modulation phase shift [16]. While there is no involuntary bulk motion in flow phantoms, our set up is very sensitive to phase shifts induced by vibration. Data where this effect was large were excluded from our analysis. OCTA flow signal was averaged inside the red circle in Fig. 3(D, E, F) for all three different techniques in order to calculate the dynamic range. In each dataset, a total of 50 averaged OCTA values were calculated for the flow rates between 0 mm/s to 6 mm/s (Fig. 3(A)). The values were normalized using the averaged saturated and minimum value in each dataset. The dynamic range is defined as the 75% in between the minimum and maximum value. A high threshold T_h and low threshold T_l is defined as the normalized values of 0.95 and

0.2, respectively. Using the PSCD method, the dynamic range of the flow detection has been improved by 33% compare the SSADA method and 17% compare to CDIF method (Fig. 3(B)).

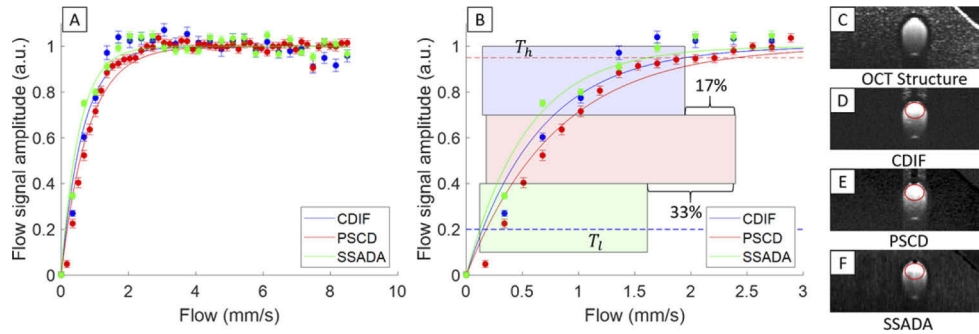


Fig. 3. Flow phantom results between three different OCTA algorithms. (A) plots of normalized OCTA values, (B) zoomed localized plots, T_h is the high threshold, T_l is the low threshold. The shaded areas indicate the dynamic range of the different methods. The red circles in D, E, and F indicate the signals used for calculating dynamic range, (C) flow phantom's OCT structure image.

3.3. Rodent imaging

PSCD, CDIF and SSADA all can generate high quality OCTA images. However, by comparing the back ground noise, we noticed that the CDIF method has a higher reflectance dependency due to the lack of intensity normalization in the OCTA algorithm (Eq. (10)). There is also some variation in image quality. In the SVP layer *en face* images (Fig. 4(A, D, G)) noise levels in the complex-based methods appear larger compared to SSADA. In the DCP layer, the PSCD and CDIF methods appear to have less noise (note the lower background in Fig. 4) compared to SSADA method. We also found that SSADA has an advantage on the superficial retinal layer and complex methods have an advantage in the deep layer for visible light OCT. In visible light data, the nerve fiber has a high reflectance and the reflectance dependency can be observed in the CDIF images. This phenomenon is more apparent in the rodent than human images. In general, the PSCD method is more suitable for rodent OCTA imaging as it can provide high image quality in both SVP and DCP. We also generated complex OCTA images without bulk motion compensation (Fig. 4(J, K, L)) and structural images for comparison (Fig. 4(M, N, O)).

3.4. Imaging using commercial OCT system

Using a commercial OCT system, all three algorithms can generate high quality OCTA images (Fig. 5). Large vessels and capillaries can be observed in three different vascular plexuses. Flow signal can also be clearly observed in B-frames (Fig. 5(G, H, I)). However, there are some differences that can be observed in the portrayal of pathologies. The patient imaged in Fig. 5 has hard exudates that can be clearly observed from fundus photo (Fig. 5(K)), OCT structural *en face* (Fig. 5(J)) and B-scans (Fig. 5(L)). These hard exudates are hyper-reflective tissues without any blood flow. Due to lack of reflectance normalization, images generated using the CDIF method (Fig. 5(E, H)). In this case, cysts with fluid that contains hyper-reflective particles can also be observed in (Fig. 5(D, E, F)).

The OCTA reflectance dependency can also be evaluated quantitatively. Here, we numerically reduced the spectrum amplitude from 100% to 10%. At every 10% reduction point, OCTA images were generated using all three different methods. *En face* inner retina angiograms were generated using maximum projection. The images were normalized from 0 to 1 according to the minimum and maximum flow pixel values generated by each method in the simulated dataset.

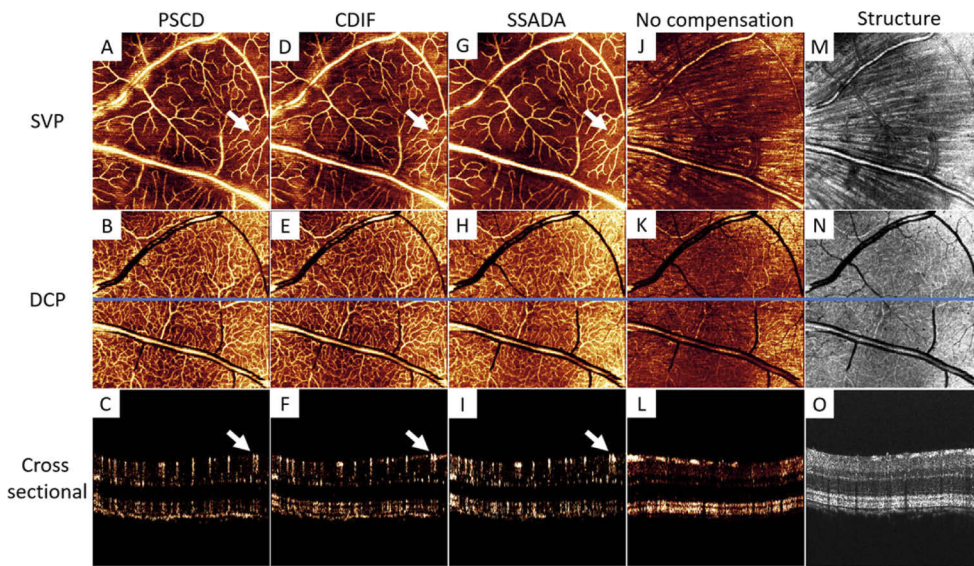


Fig. 4. OCTA images of a rat retina acquired with a visible light system compared between different algorithms. First row: superficial vascular plexus (SVP) *en face* images; second row: deep capillary plexus (DCP) *en face* images; third row: cross-sectional images selected from the same OCT/OCTA volume at the position indicated by the blue line. The CDIF method has a higher reflectance dependency, which can be observed by considering region with a high reflectance background (white arrows in D and F) than the PSCD and SSADA method (white arrows in A, C, G, I).

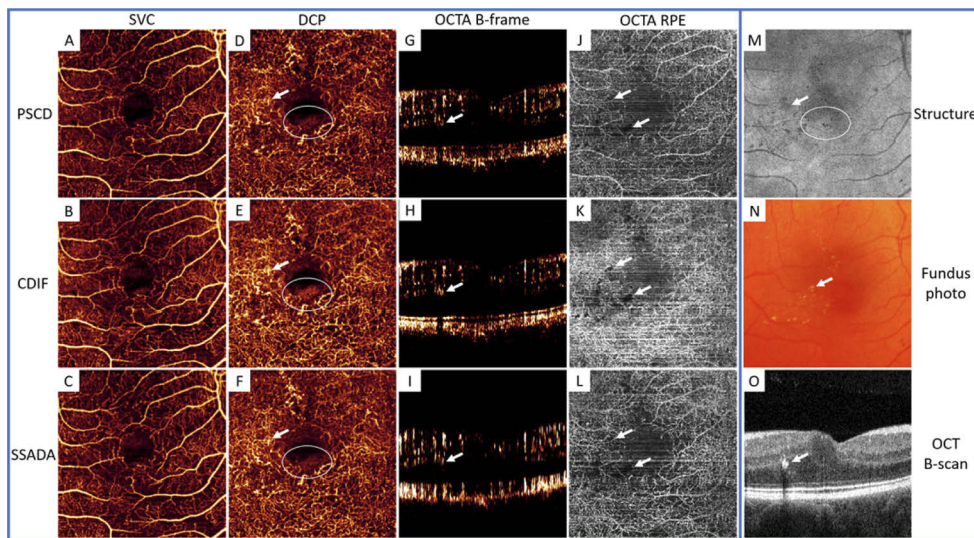


Fig. 5. OCTA image comparison between different algorithms using 3×3 mm images of an eye with diabetic retinopathy (DR). White arrows and white circles indicate the hard exudate and cystic fluid. The hard exudate and cystic fluid have higher intensity in images generated using CDIF method than the other two methods. Compare with other two method (J, L), the background noise is higher in CDIF RPE OCTA *en face* projection images (K). The CDIF method (E, H, K) has higher reflectance dependency than the other two methods (D, G, J, F, I, L).

Averaged OCTA signal intensity was calculated by averaging all pixels in the *en face* image. Due to the normalization process embedded in the decorrelation step, there is no OCTA intensity change when using PSCD or SSADA methods. However, for the CDIF method, there is a strong signal intensity dependency (blue line in Fig. 6).

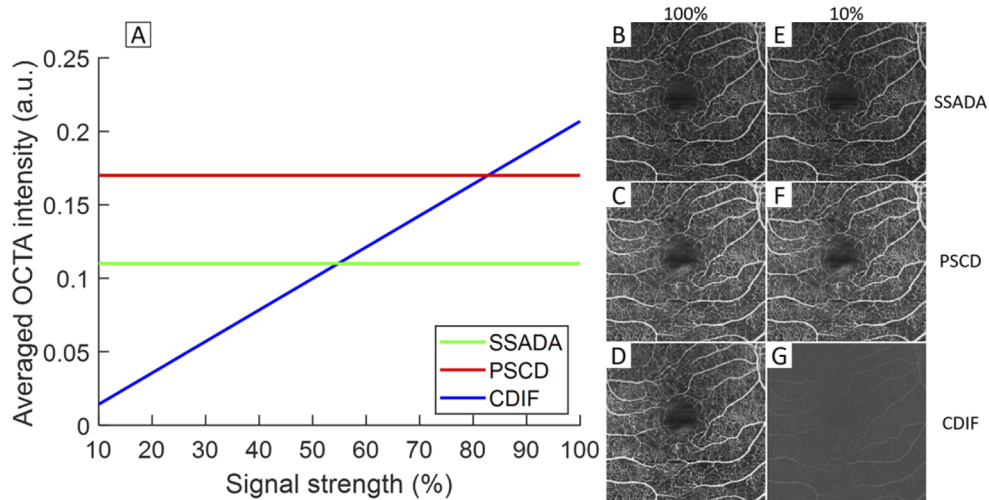


Fig. 6. Reflectance dependency compared to averaged OCTA signal intensity. Averaged OCTA signal intensity is calculated and plotted from *en face* inner retina images generated by three different OCTA methods (A). SSADA and PSCD methods have no correlation with the OCT signal intensity, but the CDIF method has high correlation with the OCT signal intensity. (B, C, D) *En face* OCTA images at 100% of signal strength, (E, F, G) *En face* OCTA images at 10% of signal strength. The flow signal is difficult to observe with the CDIF method in the low reflectance signal regime. This is clinically relevant when hyper reflective material occurs above vessels.

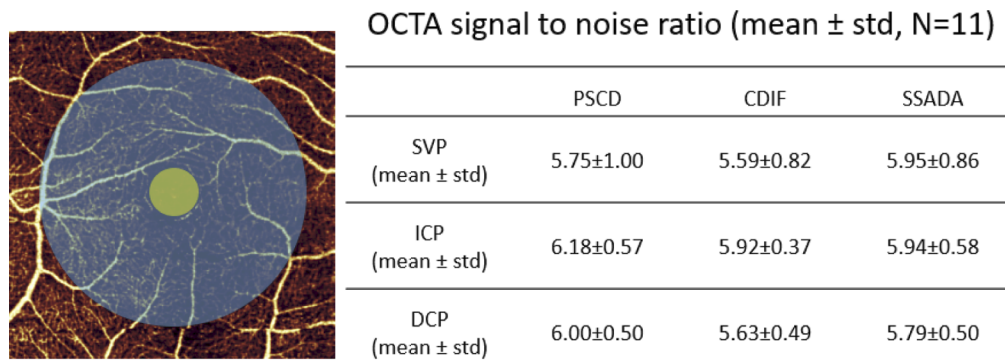


Fig. 7. Signal to noise ratio (SNR) of three OCTA algorithms, the central foveal avascular zone (FAZ) is free of blood vessels (yellow shaded area) which can be used as background noise, the parafoveal region (blue shaded area) includes high density vascular network which can be used as signal, eleven images were acquired (N=11), SNRs and their standard deviations (std) from SVP, intermediate capillary plexus (ICP) and DCP have been calculated, all three methods have comparable SNRs.

Image quality between three different methods was also investigated (Fig. 7) by calculating the signal to noise ratio (SNR) using the method introduced by Jia et al. [1] 3 × 3-mm OCTA

images were acquired from 11 healthy subjects. SVP was generated from ganglion cell layer (GCL) only, and nerve fiber layer (NFL) was excluded to avoid the potential flow artifact due to high reflectance. ICP and DCP *en face* images were also involved for this measurement. All three methods have comparable SNR values. Among them, SSADA shows higher SNR in SVP than the other two methods. PSCD shows the best image quality in ICP and DCP. This quantitative evaluation on healthy eyes is consistent to the image quality shown by eyes with diabetic retinopathy (Fig. 5).

3.5. Imaging using 400-kHz widefield OCT system

Healthy subjects and patients with diabetic retinopathy were imaged using the 400 kHz system and the PSCD method. The total data acquisition time for these images is less than one minute. The OCT and OCTA data were segmented using our previously developed automatic segmentation software [35]. The inner retinal *en face* OCTA image was generated using maximum projection (Fig. 8(A)). In the *en face* image, both large vessels and capillaries are clearly visible (Fig. 8(B-E)).

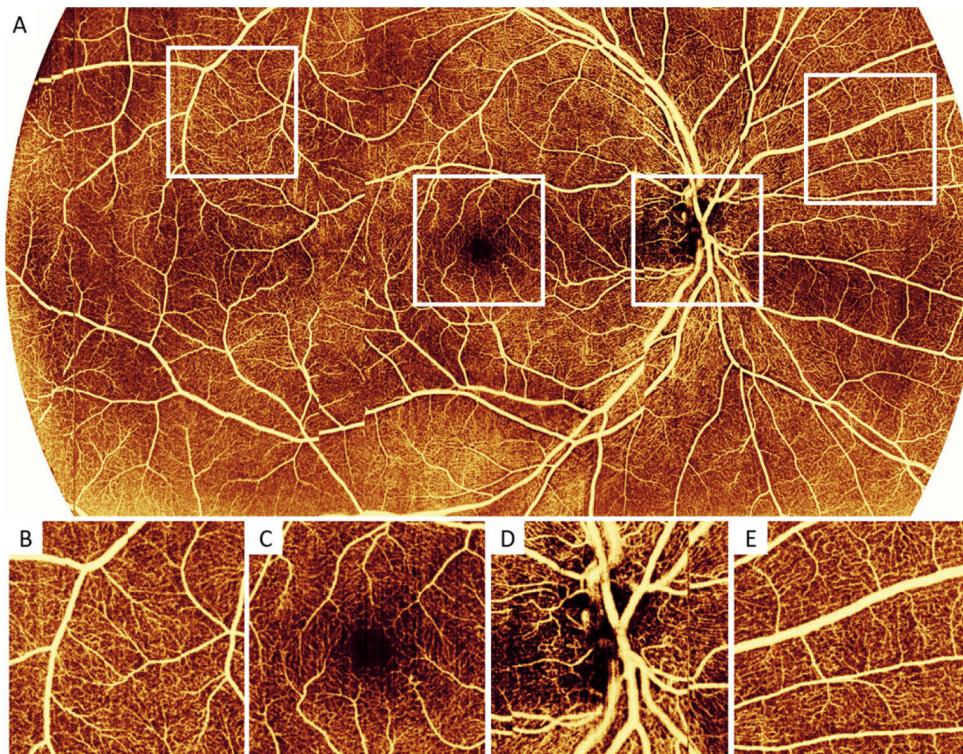


Fig. 8. wide-field PSCD OCTA image acquired from a healthy subject, (A) 12 × 23 mm wide-field PSCD OCTA image, (B-E) zoomed localized images cropped from (A).

4. Discussion

In this paper, we developed a novel PSCD angiography algorithm to generate high quality OCTA images. This algorithm incorporates an efficient and accurate phase stabilization step using a standard deviation method [16] that can be used on either spectral domain or swept source OCT systems. We evaluated its performance by assessing it on several different OCTA devices (including a visible light system) and in several different contexts (flow phantom, rodent and

human imaging). Our results show that this technique provides similar or superior imaging in these contexts as quantified by dynamic range and reflectance signal dependence.

In the *in vivo* studies presented here, the PSCD, CDIF, and SSADA methods produced adequate angiographic images. However, our PSCD method has less reflectance dependency, and both animal and human images show an improvement in image clarity. In part this is due to the fact that the PSCD method incorporates normalization into the flow signal, and in general we believe researchers should be aware of the reflectance signal dependence of the angiographic signal. If OCTA signal is high when OCT signal is high false positive flow signals can be generated. On the other hand, if OCTA signal is low when OCT signal is low, false nonperfusion region can be generated, corrupting image quantification and interpretation. As image sizes increase, vignetting, defocusing, and eye conditions such as cataract, floaters, and will become increasingly common in clinical settings. An OCTA algorithm that mitigates these effects is therefore a priority.

There are many sources of phase noise in OCTA systems. Besides bulk motion and trigger jitter, galvo jitter is another possible noise source that can significantly decrease the OCTA image quality in both spectral domain and swept source OCT systems. In our study, we didn't observe significant galvo jitter noise in either swept source or spectral domain systems. In both prototype systems, we used conventional galvo scanners with significantly higher repeatability than the system's lateral optical resolution, so lateral movement due to the galvo jitter can be safely ignored. Phase jitter, which is caused by unstable sampling and causes the spectrum to shift in phase space, is another possible noise source. Many groups have developed phase stabilization methods [26,27,36–40]. Since our PSCD method only compensates uniform phase shift and gradient phase shift caused either by bulk motion or A-scan trigger jitter, it would not be effective for removing this type of artifact. However, after we carefully calibrated our system using mirror, we nonetheless didn't observe significant phase jitter noise in this study.

Complex methods like the complex differential variance method have also been developed [41]. Unlike the complex methods used in this study, the bulk motion compensation step was integrated into this method. However, the lack of bulk motion compensation step will introduce an additional variable that may cause significant image quality differences between these methods. Based on this, in this study, we only compare the CDIF and PSCD methods, which have similar data processing procedures. SSADA as an amplitude-based method was also included in this study to highlight the significance of the phase signal.

This study has some limitations. To quantify the dynamic range of the PSCD method, we performed a flow phantom experiment, but we didn't perform a dynamic range evaluation *in vivo*. Dynamic range evaluation requires a highly accurate flow speed measurements, which are difficult to measure in retina. Without accurate flow speed, the dynamic range will be similarly difficult to estimate. In addition to the OCTA signal processing techniques explored in this study, hardware considerations in OCTA devices will also affect the flow signal detection. To achieve an unbiased comparison, we generated the flow signal from the same raw spectrum acquired in each experiment using the three different approaches discussed above. While the CDIF method we employed for comparison is described in the literature [7], we did not acquire data using the OCTA devices in which this approach is most often realized (i.e., in commercial instruments employing OMAG processing). It is possible that the CDIF approach is more appropriate for hardware configurations different than those we explored. Our method also has some disadvantages that need to be improved in the future studies. The OCTA signal used in PSCD method is correlated to the phase shift, so if the phase shift is equal or close to zero the OCTA value will still be suppressed even in the presence of speckle variance. However, in reality, due to the long inter B-scan time, the phase shift is not zero even in the transverse direction, so we expect the final image quality won't be too adversely affected.

5. Conclusion

In this paper, a novel PSCD OCTA algorithm has been successfully developed. The dynamic range has been studied using a flow phantom experiment. A high dynamic range is achieved compared to a conventional complex OCTA algorithm. This method has been tested using three different OCT systems. Image quality has been compared in three different algorithms. Quantitative analysis of the reflectance dependency was provided by numerical reduction of the reflectance signal. Our results indicate that the PSCD method obtains a higher dynamic range with less reflectance signal dependence in diverse circumstances than the alternative methods in many, though not all, circumstances.

Funding. National Institutes of Health (P30 EY010572, R01 EY024544, R01 EY027833, R01 EY031394); Research to Prevent Blindness (unrestricted departmental funding grant, William & Mary Greve Special Scholar Award); BrightFocus Foundation (G2020168).

Disclosures. Oregon Health & Science University (OHSU), Yali Jia and Xiang Wei have a significant financial interest in Optos, Inc. Oregon Health & Science University (OHSU) and Yali Jia have a significant financial interest in Optovue, Inc. These potential conflicts of interest have been reviewed and managed by OHSU.

References

1. Y. Jia, O. Tan, J. Tokayer, B. Potsaid, Y. Wang, J. J. Liu, M. F. Kraus, H. Subhash, J. G. Fujimoto, J. Horngger, and H. David, "Split-spectrum amplitude-decorrelation angiography with optical coherence tomography," *Opt. Express* **20**(4), 4710–4725 (2012).
2. S. Makita, Y. Hong, M. Yamanari, T. Yatagai, and Y. Yasuno, "Optical coherence angiography," *Opt. Express* **14**(17), 7821–7840 (2006).
3. L. An and R. K. Wang, "In vivo volumetric imaging of vascular perfusion within human retina and choroids with optical micro-angiography," *Opt. Express* **16**(15), 11438–11452 (2008).
4. A. Mariampillai, M. K. Leung, M. Jarvi, B. A. Standish, K. Lee, B. C. Wilson, A. Vitkin, and V. X. Yang, "Optimized speckle variance OCT imaging of microvasculature," *Opt. Lett.* **35**(8), 1257–1259 (2010).
5. J. Fingler, D. Schwartz, C. Yang, and S. E. Fraser, "Mobility and transverse flow visualization using phase variance contrast with spectral domain optical coherence tomography," *Opt. Express* **15**(20), 12636–12653 (2007).
6. T. E. De Carlo, A. Romano, N. K. Waheed, and J. S. Duker, "A review of optical coherence tomography angiography (OCTA)," *Int. J. Retin. Vitr.* **1**(1), 5 (2015).
7. R. K. Wang, S. L. Jacques, Z. Ma, S. Hurst, S. R. Hanson, and A. Gruber, "Three dimensional optical angiography," *Opt. Express* **15**(7), 4083–4097 (2007).
8. R. A. Leitgeb, R. M. Werkmeister, C. Blatter, and L. Schmetterer, "Doppler optical coherence tomography," *Prog. Retinal Eye Res.* **41**, 26–43 (2014).
9. R. A. Leitgeb, L. Schmetterer, C. K. Hitzenberger, A. F. Fercher, F. Berisha, M. Wojtkowski, and T. Bajraszewski, "Real-time measurement of in vitro flow by Fourier-domain color Doppler optical coherence tomography," *Opt. Lett.* **29**(2), 171–173 (2004).
10. J. D. Briers, "Laser Doppler and time-varying speckle: a reconciliation," *J. Opt. Soc. Am. A* **13**(2), 345–350 (1996).
11. J. D. Briers, "Speckle fluctuations and biomedical optics: implications and applications," *Opt. Eng.* **32**(2), 277–283 (1993).
12. J. M. Schmitt, S. Xiang, and K. M. Yung, "Speckle in optical coherence tomography," *J. Biomed. Opt.* **4**(1), 95–105 (1999).
13. S. B. Ploner, E. M. Moult, W. Choi, N. K. Waheed, B. Lee, E. A. Novais, E. D. Cole, B. Potsaid, L. Husvogt, and J. Schottenhamml, "Toward quantitative OCT angiography: visualizing blood flow speeds in ocular pathology using variable interscan time analysis (VISTA)," *Retina* **36**(Supplement 1), S118–S126 (2016).
14. W. Choi, E. M. Moult, N. K. Waheed, M. Adhi, B. Lee, C. D. Lu, E. Talisa, V. Jayaraman, P. J. Rosenfeld, and J. S. Duker, "Ultrahigh-speed, swept-source optical coherence tomography angiography in nonexudative age-related macular degeneration with geographic atrophy," *Ophthalmology* **122**(12), 2532–2544 (2015).
15. X. Wei, T. T. Hormel, S. Pi, Y. Guo, Y. Jian, and Y. Jia, "High dynamic range optical coherence tomography angiography (HDR-OCTA)," *Biomed. Opt. Express* **10**(7), 3560–3571 (2019).
16. X. Wei, A. Camino, S. Pi, W. Cepurna, D. Huang, J. C. Morrison, and Y. Jia, "Fast and robust standard-deviation-based method for bulk motion compensation in phase-based functional OCT," *Opt. Lett.* **43**(9), 2204–2207 (2018).
17. G. Liu, O. Tan, S. S. Gao, A. D. Pechauer, B. Lee, C. D. Lu, J. G. Fujimoto, and D. Huang, "Postprocessing algorithms to minimize fixed-pattern artifact and reduce trigger jitter in swept source optical coherence tomography," *Opt. Express* **23**(8), 9824–9834 (2015).
18. S. Song, J. Xu, S. Men, T. T. Shen, and R. K. Wang, "Robust numerical phase stabilization for long-range swept-source optical coherence tomography," *J. Biophotonics* **10**(11), 1398–1410 (2017).
19. A. F. Fercher, C. K. Hitzenberger, G. Kamp, and S. Y. El-Zaiat, "Measurement of intraocular distances by backscattering spectral interferometry," *Opt. Commun.* **117**(1-2), 43–48 (1995).

20. B. Tan, Z. Hosseinaee, L. Han, O. Kralj, L. Sorbara, and K. Bizheva, “250 kHz, 1.5 μm resolution SD-OCT for in-vivo cellular imaging of the human cornea,” *Biomed. Opt. Express* **9**(12), 6569–6583 (2018).
21. T. C. Chen, B. Cense, M. C. Pierce, N. Nassif, B. H. Park, S. H. Yun, B. R. White, B. E. Bouma, G. J. Tearney, and J. F. De Boer, “Spectral domain optical coherence tomography: ultra-high speed, ultra-high resolution ophthalmic imaging,” *Arch. Ophthalmol.* **123**(12), 1715–1720 (2005).
22. T. Klein, W. Wieser, C. M. Eigenwillig, B. R. Biedermann, and R. Huber, “Megahertz OCT for ultrawide-field retinal imaging with a 1050 nm Fourier domain mode-locked laser,” *Opt. Express* **19**(4), 3044–3062 (2011).
23. R. Huber, M. Wojtkowski, and J. Fujimoto, “Fourier Domain Mode Locking (FDML): A new laser operating regime and applications for optical coherence tomography,” *Opt. Express* **14**(8), 3225–3237 (2006).
24. L. An, J. Qin, and R. K. Wang, “Ultrahigh sensitive optical microangiography for in vivo imaging of microcirculations within human skin tissue beds,” *Opt. Express* **18**(8), 8220–8228 (2010).
25. Z. Chen, M. Liu, M. Minneman, L. Ginner, E. Hoover, H. Sattmann, M. Bonesi, W. Drexler, and R. A. Leitgeb, “Phase-stable swept source OCT angiography in human skin using an akinetic source,” *Biomed. Opt. Express* **7**(8), 3032–3048 (2016).
26. W. Choi, B. Potsaid, V. Jayaraman, B. Baumann, I. Grulkowski, J. J. Liu, C. D. Lu, A. E. Cable, D. Huang, and J. S. Duker, “Phase-sensitive swept-source optical coherence tomography imaging of the human retina with a vertical cavity surface-emitting laser light source,” *Opt. Lett.* **38**(3), 338–340 (2013).
27. B. Braaf, K. A. Vermeer, V. A. D. Sicam, E. van Zeeburg, J. C. van Meurs, and J. F. de Boer, “Phase-stabilized optical frequency domain imaging at 1- μm for the measurement of blood flow in the human choroid,” *Opt. Express* **19**(21), 20886–20903 (2011).
28. S. S. Gao, G. Liu, D. Huang, and Y. Jia, “Optimization of the split-spectrum amplitude-decorrelation angiography algorithm on a spectral optical coherence tomography system,” *Opt. Lett.* **40**(10), 2305–2308 (2015).
29. X. Wei, T. T. Hormel, Y. Guo, and Y. Jia, “75-degree non-mydriatic single-volume optical coherence tomographic angiography,” *Biomed. Opt. Express* **10**(12), 6286–6295 (2019).
30. X. Wei, A. Camino, S. Pi, T. T. Hormel, W. Cepurna, D. Huang, J. C. Morrison, and Y. Jia, “Real-time cross-sectional and en face OCT angiography guiding high-quality scan acquisition,” *Opt. Lett.* **44**(6), 1431–1434 (2019).
31. X. Wei, T. T. Hormel, Y. Guo, T. S. Hwang, and Y. Jia, “High-resolution wide-field OCT angiography with a self-navigation method to correct microsaccades and blinks,” *Biomed. Opt. Express* **11**(6), 3234–3245 (2020).
32. S. Pi, A. Camino, W. Cepurna, X. Wei, M. Zhang, D. Huang, J. Morrison, and Y. Jia, “Automated spectroscopic retinal oximetry with visible-light optical coherence tomography,” *Biomed. Opt. Express* **9**(5), 2056–2067 (2018).
33. M. Zhang, J. Wang, A. D. Pechauer, T. S. Hwang, S. S. Gao, L. Liu, L. Liu, S. T. Bailey, D. J. Wilson, and D. Huang, “Advanced image processing for optical coherence tomographic angiography of macular diseases,” *Biomed. Opt. Express* **6**(12), 4661–4675 (2015).
34. T. T. Hormel, J. Wang, S. T. Bailey, T. S. Hwang, D. Huang, and Y. Jia, “Maximum value projection produces better en face OCT angiograms than mean value projection,” *Biomed. Opt. Express* **9**(12), 6412–6424 (2018).
35. Y. Guo, A. Camino, M. Zhang, J. Wang, D. Huang, T. Hwang, and Y. Jia, “Automated segmentation of retinal layer boundaries and capillary plexuses in wide-field optical coherence tomographic angiography,” *Biomed. Opt. Express* **9**(9), 4429–4442 (2018).
36. S. Moon and Z. Chen, “Phase-stability optimization of swept-source optical coherence tomography,” *Biomed. Opt. Express* **9**(11), 5280–5295 (2018).
37. J. Xi, L. Huo, J. Li, and X. Li, “Generic real-time uniform K-space sampling method for high-speed swept-Source optical coherence tomography,” *Opt. Express* **18**(9), 9511–9517 (2010).
38. M. Gora, K. Karnowski, M. Szkulmowski, B. J. Kaluzny, R. Huber, A. Kowalczyk, and M. Wojtkowski, “Ultra high-speed swept source OCT imaging of the anterior segment of human eye at 200 kHz with adjustable imaging range,” *Opt. Express* **17**(17), 14880–14894 (2009).
39. S. Kim, P. D. Raphael, J. S. Oghalai, and B. E. Applegate, “High-speed spectral calibration by complex FIR filter in phase-sensitive optical coherence tomography,” *Biomed. Opt. Express* **7**(4), 1430–1444 (2016).
40. B. Vakoc, S.-H. Yun, J. De Boer, G. Tearney, and B. Bouma, “Phase-resolved optical frequency domain imaging,” *Opt. Express* **13**(14), 5483–5493 (2005).
41. A. S. Nam, I. Chico-Calero, and B. J. Vakoc, “Complex differential variance algorithm for optical coherence tomography angiography,” *Biomed. Opt. Express* **5**(11), 3822–3832 (2014).